High-Performance Perovskite-Inspired Lanthanohalide Memristors for Phototunable Neuromorphic Applications

Manvendra Chauhan and Satinder K. Sharma Sr., *Member, IEEE*

***Abstract*— Nonvolatile memory (NVM) devices that can respond to optical stimuli are emerging as key enablers for next-generation neuromorphic computing, integrating optical and electronic functionalities. Among the materials being explored, perovskite has emerged as a standout candidate for optically active resistive random access memory (ReRAM). However, a major hurdle remains: the long-term stability of the switching layer (SL). In light of this, we present a lead-free and highly stable novel $AgEuBr_4$ perovskite-like lanthanohalide, designed specifically to serve as an SL for electro-optical ReRAMs. The $AgEuBr_4$ thin films were deposited using a one-step spin-coating method on FTO substrates and subsequently annealed at 260 °C. To further enhance performance, a ∼10-nm HfO_X passivation layer is applied via atomic layer deposition (ALD). The Ag top electrodes (TEs) were patterned using an in-house dry-etching technique. The fabricated ReRAM devices displayed impressive bipolar NVM behavior under both dark conditions and ultraviolet (UV) ($\lambda = 365$ nm) irradiation. When operated under UV irradiation, the ReRAM devices exhibit two more resistive states distinct from the dark condition operation while operating at lower voltages (±0.30 V) and ultrafast switching duration of 10.07 ns, ensuring energy efficiency and fast data processing. Also, a high low-resistance state (LRS)/HRS ratio (∼9526.35), excellent endurance (51 696 cycles), and robust retention (62 986 s) under UV irradiation set a new standard in performance. Furthermore, phototunable neuromorphic behavior was validated through both long-term potentiation (LTP), short-term plasticity (STP), and paired-pulse facilitation (PPF)% measurements, where the device exhibited significantly enhanced conductance modulation and synaptic facilitation under UV exposure, highlighting its applicability in light-assisted neuromorphic computing.**

***Index Terms*— Lead-free, neuromorphic, optically-tunable, perovskite, resistive memory.**

I. Introduction

IN RECENT years, remarkable breakthroughs in materials engineering have been directed toward optimizing perovskite-based architectures to improve photostability, moisture resistance, and overall performance in optically active resistive random access memory (ReRAM) devices [1], [2], [3]. These innovative perovskite-based devices offer promising neuromorphic functionalities due to their intrinsic opto-electronic coupling and low-voltage operations. However, despite substantial strides in enhancing device robustness, conventional lead (Pb)-based perovskites, both 3-D and 2-D organometal halide variants, continue to dominate high-performance optoelectronic applications. Their superior defect tolerance, carrier mobility, and broad absorption properties are hard to match [4], [5], [6].

Nevertheless, the inherent toxicity of lead raises significant environmental and health concerns, especially amid strict global regulations. This has accelerated the transition toward lead-free alternatives, catalyzing a vibrant research effort aimed at developing and integrating environmentally benign materials that retain the exceptional optoelectronic properties of conventional perovskite systems.

Among the most actively explored strategies is the monovalent substitution of Pb^{2+} with trivalent cations exhibiting comparable ionic radii and stable oxidation states. Elements, such as tin (Sn^{2+}), bismuth (Bi^{3+}), and antimony (Sb^{3+}), preferably fit this criterion and show favorable chemical stability and optoelectronic performance [7]. Recent developments in lead-free halide-based resistive switching (RS) systems, including Bi-based, $Cs_3Bi_2X_9$ perovskite-like thin films [8] and Sn-based, $MASnI_3$, and $PEACl/MASnI_3$ [9], have demonstrated the viability of RS operations and analog plasticity for neuromorphic computing. However, due to their distinct valence states, Bi- and Sb-based halide compounds typically do not adopt the conventional ABX_3 perovskite structure, leading to alternative crystallographic frameworks with distinct transport and electronic properties. Moreover, the quest for uniform, high-quality thin films of these materials at scale remains challenging due to issues in film crystallinity, large-area uniformity, and defect density. These factors can greatly influence the variability of electrical switching behavior, endurance, and stability [10]. Overcoming these hurdles is not just a matter of scientific advancement; it is essential for realizing the full potential of next-generation optoelectronic devices. The shift toward safer, more sustainable

Received 1 May 2025; revised 19 June 2025; accepted 24 June 2025. Date of publication 8 July 2025; date of current version 25 July 2025. The review of this article was arranged by Editor X. Liu. *(Corresponding author: Satinder K. Sharma.)*

The authors are with the School of Computing and Electrical Engineering (SCEE), IIT Mandi, Mandi, Himachal Pradesh 175075, India (e-mail: satinder@iitmandi.ac.in).

Digital Object Identifier 10.1109/TED.2025.3584289

materials could redefine the industry and usher in a new era of innovation.

A revolutionary class of materials is emerging, capturing significant attention: trivalent lanthanide (Ln^{3+}) ions, particularly europium (Eu^{3+}) [11], [12], which exhibit a comparable ionic radius to Pb^{2+} and offer enhanced chemical and photostability. Notably, Eu^{3+} possesses a significantly lower oxidation potential (−0.34 V) compared to other lanthanide ions and group VA alternatives, significantly diminishing its vulnerability to redox-induced degradation within a perovskite lattice, while Eu-based compounds do not form traditional perovskite structures due to their oxidation state mismatch, ingeniously integrated into a new generation of perovskite-inspired materials, showcasing remarkable light-harvesting and resistive-switching capabilities [13], [14].

Among these innovations, particular interest is pnictogen-integrated silver (Ag^+) and copper (Cu^+)-based pnictohalides, with a general stoichiometry of $A_xB_yX_{x+3y}$, where $A^+ = Ag^+$ or Cu^+, $B^{3+} = Bi^{3+}$, or Sb^{3+}, and $X^- = I^-$ or Br^- [15].

These materials, including variations of the intriguing "rudorffite" structure, demonstrate impressive traits such as high photocarrier mobility, tunable bandgaps, exceptional photostability, and enhanced switching dynamics under optical stimuli. Their inherent ionic conductivity and photoresponsive RS make them highly promising candidates for next-generation ReRAM and neuromorphic computing applications. Substituting traditional group VA elements with Ln ions such as Eu^{3+} provides more sustainability to the aforementioned stoichiometry due to similar ionic radii and comparatively lower oxidation potential.

Therefore, in this study, we report the synthesis and integration of a novel perovskite-inspired lanthanohalide, $AgEuBr_4$, employed as the active switching layer (SL) in an advanced phototunable ReRAM architecture. The $AgEuBr_4$ thin films were expertly deposited via spin-coating on FTO-coated glass substrates and subsequently passivated with a conformal HfO_X layer using atomic layer deposition (ALD) technology. This passivation step significantly enhanced surface stability and effectively suppressed undesirable ion migration phenomena. Through meticulous photolithographic patterning and reactive ion etching (RIE), we fabricated a sophisticated device structure, $Ag/HfO_X/AgEuBr_4/FTO$, with clearly defined top electrodes (TEs). ALD HfO_X films possess terminal –OH groups and Hf^{4+} ions during growth, which chemically interact with surface defects such as partially under-coordinated (particularly Ag+ or Eu^{3+}) and halide vacancies (especially Br^-) and halogen-rich antisite defects [16], [17], [18]. In the context of $AgEuBr_4$ SL, these defects, typically acting as shallow trap states, nonuniform switching, and leakage pathways, are effectively passivated via coordinate bonding between Hf^{4+}ions and nonstoichiometric surface sites, including Br^- vacancies and undercoordinated Eu^{3+} ions. This interaction results in the formation of stable Hf–O–Br and Hf–O–Eu linkages at the interface, significantly neutralizing trap states and minimizing nonradiative recombination. This passivation mechanism mirrors that observed in perovskite solar cells, where ALD-grown HfO_X has been shown to significantly suppress surface recombination by bonding to halide-related vacancies and dangling bonds [16], [17], [18]. This targeted passivation substantially reduces parasitic leakage currents and mitigates uncontrolled ion migration, thereby enabling cleaner and more reproducible filament formation and rupture events, resulting in distinctly stable resistive states. Similar passivation strategies have demonstrated success in enhancing both stability and performance in various perovskite-based device systems [19].

The fabricated devices exhibited impressively reproducible and stable RS characteristics under both dark and ultraviolet (UV) irradiation ($\lambda = 365$ nm). Under UV exposure, the ReRAM exhibited a significantly reduced SET voltage (V_S) and RESET voltage (V_R) of +0.30 and −0.30 V, respectively, with enhanced switching uniformity. The UV-irradiated devices retained a high low-resistance state (LRS)/HRS ratio (∼9526.35) and maintained stable LRSs over 62 986-s durations. The underlying switching mechanism is attributed to the dynamic formation and rupture of silver-based conductive filaments (CFs) across the $AgEuBr_4$ layer, mimicking ion transport phenomena akin to biological synapses, particularly the Na^+ influx responsible for signal transmission in neural networks. These extraordinary results underscore the transformative potential of lanthanohalide-based perovskite-inspired systems as a viable platform for bio-mimetic optoelectronic devices. The intrinsic phototunability, low-voltage operation, and synapse-analogous behavior of the proposed $AgEuBr_4$ ReRAM underline it as a game-changing solution for energy-efficient, optically modulated neuromorphic computing architectures.

II. Experimental Section

Europium (III) bromide hydrate (EuBr3; ≥99.99%), silver bromide (AgBr; ≥98%), and N,N-dimethylformamide (DMF) were purchased from Sigma-Aldrich and were used as received without any further processing.

Novel $AgEuBr_4$ lanthanohalide was synthesized via a single-step, solution-based process. Equimolar amounts of AgBr and $EuBr_3$ precursors were mixed in a 1:1 molar ratio and dissolved in DMF. The resulting solution was continuously stirred at 70 °C for 8 h. Initially, the mixture appeared greenish-yellow; however, it gradually transitioned to a transparent solution over time, completing the $AgEuBr_4$ lanthanohalide formulation.

Thin-film deposition was subsequently carried out using the spin-coating technique. Commercial FTO-coated glass substrates were used as BE. Prior to film deposition, the FTO substrates were sequentially ultrasonicated in deionized water, acetone, and isopropanol for 15 min each. This was followed by a 30-min UV/ozone surface treatment to enhance film adhesion and surface energy. The freshly prepared $AgEuBr_4$ precursor solution was spin-coated onto the precleaned FTO substrates at 4000 r/min for 45 s. Toluene was applied as an antisolvent during the spin process to induce rapid crystallization. The as-deposited films were initially dried at 120 °C for 20 min and then subjected to a postannealing treatment at 260 °C for 10 min to improve crystallinity and remove residual solvents. All solution preparation and film processing steps

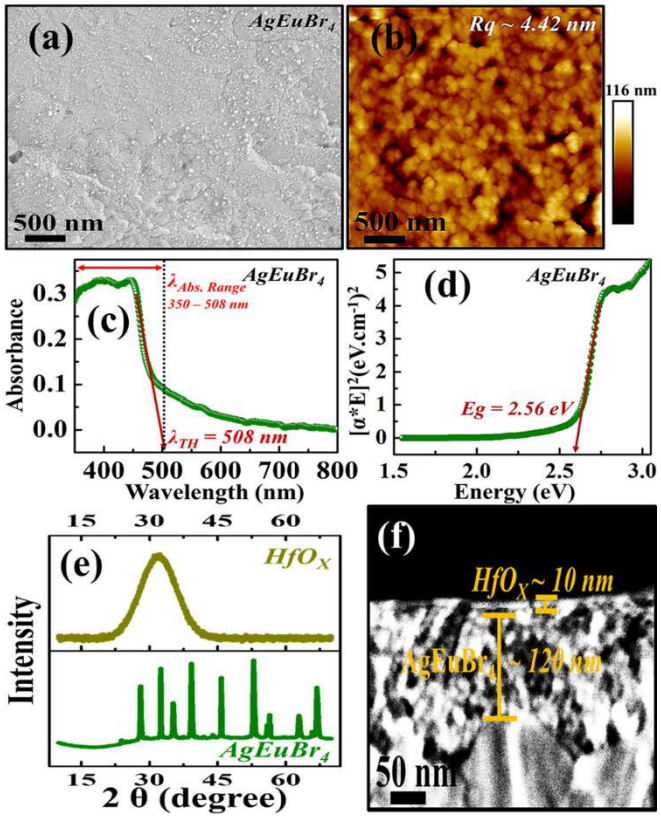

Fig. 1. (a) FESEM micrograph of the $AgEuBr_4$ surface. (b) AFM topography image of the $AgEuBr_4$ surface. (c) UV–Vis absorption spectra of the $AgEuBr_4$/FTO film. (d) Tauc plot for optical bandgap estimation of $AgEuBr_4$/FTO. (e) XRD patterns of $AgEuBr_4$/FTO and HfO_X/$AgEuBr_4$. (f) Cross-sectional FESEM image of the HfO_X/$AgEuBr_4$/FTO stack.

were conducted inside a glovebox's inert nitrogen atmosphere to prevent moisture and oxygen contamination. The final thickness of the $AgEuBr_4$ films was measured to be ~120 nm under a stylus profilometer.

To enhance the device stability and suppress interface-induced degradation, the $AgEuBr_4$ thin films were passivated with a ~10-nm-thick HfO_X film, deposited via ALD at the process temperature of 120 °C. Subsequently, Ag was deposited as TE over the HfO_X/$AgEuBr_4$/FTO stack. The TE patterning was performed using standard photolithography followed by RIE, as described in detail in Section III. The final device architecture, Ag/HfO_X/$AgEuBr_4$/FTO, was thus realized, where FTO serves as the BE and Ag as TE in the ReRAM configuration.

III. Results and Discussion

The surface morphology and uniformity coverage of the spin-coated $AgEuBr_4$ lanthanohalide thin film on FTO substrates were systematically examined using field-emission scanning electron microscopy (FESEM). As depicted in Fig. 1(a), the FESEM micrograph reveals a continuous, pinhole-free film with uniform surface coverage, indicating the high quality of the deposition process. Such morphological consistency is vital for ensuring stable and reproducible RS performances of the developed ReRAM devices.

To further evaluate deeper insight into the topography and nanoscale roughness (Rq) of the $AgEuBr_4$ SL, atomic force microscopy (AFM) was employed in tapping mode. The AFM analysis revealed a surface Rq of ~4.42 nm, as shown in Fig. 1(b). The low Rq value (Rq ~ 4.42 nm) of the deposited $AgEuBr_4$ suggests good film compactness, conducive to fostering the reliable interface formation with the HfO_X passivation layer, which is essential for ensuring stable and consistent reproducible switching operations. To assess the optical properties pivotal for phototunable switching, UV–vis absorption spectroscopy was performed on freshly deposited $AgEuBr_4$ films. As illustrated in Fig. 1(c), the material exhibits a distinct absorption peak (λpeak) centered around 446 nm. Furthermore, the broader absorption window ranging from 340 to 487 nm (λAbs.range) confirms the suitability of the $AgEuBr_4$ thin film for UV-activated optoelectronic applications. The optical bandgap energy (Eg) calculated as 2.56 eV using the tauc plot, presented in Fig. 1(d), is also in agreement with the similar type of perovskite-inspired light harvesting inorganic materials [8], [15].

The X-ray diffraction (XRD) patterns of the deposited $AgEuBr_4$SL and ALD deposited $HfO_X$are shown in Fig. 1(e). For the $AgEuBr_4$ film deposited over the FTO substrate, distinct and sharp diffraction peaks were observed at 2θ angles of 28.14°, 32.40°, 45.98°, 56.64°, and 66.93°. These peaks correspond to shifted (111), (200), (220), (400), and (640) planes, respectively, compared to the characteristic planes of pristine AgBr crystals, typically located at 26.73°, 30.96°, 44.35°, 55.04°, and 66.48° 2θ positions [20], [21]. The observed shift indicates possible lattice distortion or compositional modification induced by the incorporation of Eu^{3+} ions into the AgBr framework, leading to the formation of the $AgEuBr_4$ phase. Additional diffraction peaks detected at 35.62° and 53.46° are attributed to the underlying FTO substrate [JCPDS card no. 41–1445], which serves as the BE in the ReRAM configuration.

In contrast, the XRD pattern of the ALD-deposited HfO_X layer exhibited a broad, low-intensity hump centered around 32°, characteristic of an amorphous structure [22]. The HfO_X layer (~10 nm) was intentionally deposited at a low processing temperature of 120 °C without any postdeposition annealing, specifically to retain its amorphous nature. Maintaining the amorphous state minimizes grain boundary formation, thereby suppressing potential leakage pathways [23]. In addition, the amorphous nature of the HfO_X film contributes to long-term interfacial stability by forming a chemically inert and defect-suppressing layer, which inhibits regeneration of surface traps, a behavior analogous to HfO_X passivation of silicon interfaces in photoelectrochemical systems [16]. The low-temperature ALD process helps to mitigate interfacial diffusion and suppress stress-induced defect formation at the HfO_X/$AgEuBr_4$ interface. Avoiding high-temperature annealing prevents thermal degradation of the underlying $AgEuBr_4$ layer, which is susceptible to halide volatilization and phase instability under elevated thermal budgets.

A cross-sectional FESEM image of the HfO_X/$AgEuBr_4$ stack on the FTO-coated glass substrate, presented in Fig. 1(c), confirms the layered structure and validates the precise film

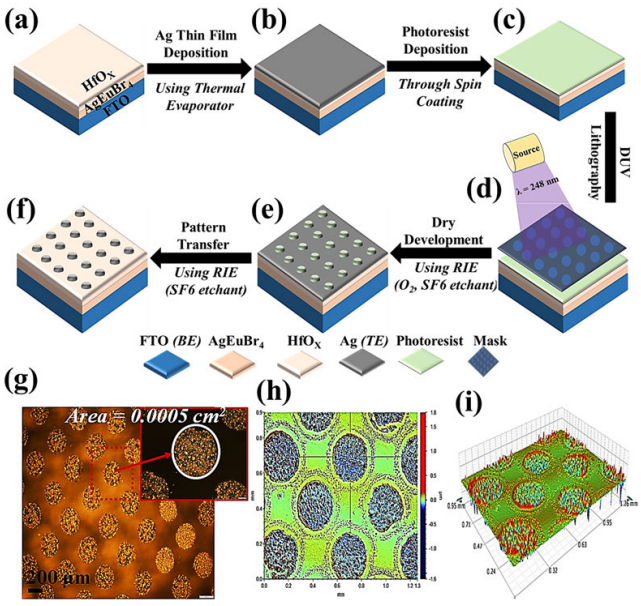

Fig. 2. (a) 3-D schematic illustration of HfOX/AgEuBr4/FTO stack. (b)–(f) Standard electrode patterning process through DUV lithography using dry development of exposed PR and pattern transfer. (g) Optical micrograph of patterned Ag electrode over HfOX/AgEuBr4/FTO stack. (h) Planar optical profilometry map of a patterned electrode. (f) 3-D surface profilometry view of the patterned electrode.

thicknesses. The $AgEuBr_4$ thin layer was measured to be ~120 nm thick, while the thickness of the conformal HfO_X layer was ~10 nm.

Given the overlap between the material's absorption characteristics and available standard UV light source facility, a wavelength of 365 nm was strategically selected for further investigation of the phototunable RS performance of the fabricated Ag/HfO_X/$AgEuBr_4$/FTO ReRAM devices. The excitation wavelength chosen is firmly well within the absorption range of the $AgEuBr_4$ SL, ensuring efficient photogeneration of carriers and effective modulation of CF dynamics under UV illumination.

Following successful morphological and topographical characterization of the $AgEuBr_4$ thin films, TE patterning was performed over the HfO_X/$AgEuBr_4$/FTO stack using a lithography-assisted pattern transfer process, as illustrated in Fig. 2. Initially, Ag thin films with an average thickness of ~110 nm were deposited via thermal evaporation onto the HfO_X-passivated $AgEuBr_4$ layer [see Fig. 2(a-b)]. To accurately define the device geometry, an in-house-designed and developed negative photoresist (PR) layer (~120 nm) was spin-coated onto the Ag surface [see Fig. 2(c)]. The PR was based on an indigenously developed metal-organic cluster (MOC) formulation: indium methacrylate (In-MAA, InC14H18O8) [24]. The MOC-based state-of-the-art PR exhibits higher resistance to plasma etching agents due to its ability to undergo photo-induced crosslinking during lithographic exposure [25].

Photolithographic patterning was carried out using a 248-nm deep ultraviolet (DUV) source and a photomask containing a 250-μm-diameter circular matrix [see Fig. 2(d)]. Upon exposure, the MOC clusters within the In-MAA PR undergo localized cross-linking, resulting in hardened regions that are highly resistant to subsequent plasma etching steps. In contrast, the unexposed PR regions remain soft and susceptible to being easily removed.

To effectively develop the exposed PR patterns without the use of solvents (i.e., via dry development), a sequential plasma treatment process was employed. Initially, O_2 plasma, at 2.6×10^4 mbar and 20-W RF, was used to decompose the organic moieties in the unexposed MOC PR. This was followed by SF_6 plasma exposure at 4.5×10^4 mbar and 45-W RF, which selectively removed the remaining inorganic components and residual organics, thereby achieving complete removal of the unexposed PR areas [see Fig. 2(e)].

Subsequently, in an SF_6 plasma at 4.5×10^4 mbar and 45-W RF, an etching step was employed to transfer the Ag pattern beneath the exposed PR directly onto the HfO_X/$AgEuBr_4$/FTO stack [see Fig. 2(f)]. Following the Ag etching step using SF_6 plasma, the residual cross-linked PR was eliminated through a two-step indigenously standardized dry plasma ashing process for a compatible process flow for in-house designed and developed resist. Initially, O_2 plasma ashing (RF power: 25 W; pressure: 2.6×10^4 mbar; and duration: 180 s) facilitated oxidative degradation of the organic PR matrix. This was followed by Ar plasma cleaning (RF power: 20 W; pressure: 3.0×10^4 mbar; and duration: 60 s) to remove residual carbonaceous by-products and any redeposited metal-organic fragments [26]. The etching process was precisely controlled to ensure clean, well-defined Ag electrodes, with a diameter measured as 250 μm, with minimal damage to the underlying layers. All fabrication steps, including PR coating, exposure, plasma development, and metal patterning, were conducted in a controlled cleanroom environment to ensure reproducibility and prevent contamination. Importantly, no wet development was involved at any stage, preserving the integrity of the $AgEuBr_4$ thin film and the integrity of its interfaces.

The optical micrograph of the patterned Ag circular electrodes (250 μm diameter) on the HfO_X/$AgEuBr_4$/FTO substrate, as shown in Fig. 2(g), confirms the successful implementation of the fully dry, plasma-based lithography and etching process. However, the presence of minor residual PR observed on the TE surface in Fig. 2(i) may marginally influence contact resistance but is not expected to significantly impact charge carrier injection or overall device performance. The thickness of the Ag TEs was measured to be ~85 nm, as determined by optical profilometry mapping. Both planar and 3-D optical profilometer images of the patterned electrodes are presented in Fig. 2(h) and (i). Here, each patterned circular Ag electrode matrix over the HfO_X/$AgEuBr_4$/FTO stack represents a single ReRAM device with an area measured as 0.0005 cm^2.

These findings reinforce the effectiveness of the indigenously custom-developed, solvent-free lithography process protocols in achieving high-resolution electrode features compatible and suitable for optoelectronic and nanoscale memory device fabrication. The same fabrication process protocol was also employed for the nonpassivated $AgEuBr_4$-based ReRAM device configuration (Ag/$AgEuBr_4$/FTO) and the ReRAM

devices employing platinum (Pt) as TE to facilitate a comprehensive and accurate comparison of RS performance with the passivated $AgEuBr_4$-based ReRAM devices. This approach ensures consistency in process parameters, thereby minimizing variations and enhancing the reliability of the comparative analysis.

The resistive performances of passivated and nonpassivated $AgEuBr_4$-based ReRAM devices are compared in Fig. 3. All RS characterizations were performed under controlled ambient conditions, specifically at a relative humidity of ∼45% and a temperature of ∼21 °C within the Class 100 Cleanroom Facility (C4DFED, IIT Mandi). The nonpassivated $Ag/AgEuBr_4/FTO$ configuration exhibited an LRS/HRS ratio of ∼859.09, switching from HRS to LRS at an SET voltage (V_S) of +0.28 V and reverting back to HRS at an RESET voltage (V_R) of −0.36 V [see Fig. 3(a)]. In contrast, the passivated $Ag/HfO_X/AgEuBr_4/FTO$ configuration, featuring an HfO_X passivation layer, demonstrated a significantly improved LRS/HRS ratio of ∼5897.04, albeit with slightly increased switching voltages of +0.48 V (V_S) and −0.48 V (V_R) [see Fig. 3(b)]. This marked enhancement in the LRS/HRS ratio for the passivated configuration can be attributed to effective suppression of surface states and defect densities by the HfO_X passivation layer. Such surface passivation aligns with prior studies, which established that interfacial passivation layers significantly mitigate surface traps [1], [23], [27], thus reducing stochastic behavior in CF formation and rupture processes. Endurance tests, illustrated in Fig. 3(c), further validate these improvements. Specifically, the nonpassivated device experienced noticeable degradation after approximately 27 543 resistive cycles, likely due to increased ion diffusion and CF instability. Conversely, the passivated device maintained clear and distinct LRS/HRS states throughout 51 696 cycles, [see Fig. 3(d)] effectively doubling the operational lifespan while ensuring stable switching behavior. These findings corroborate previous reports emphasizing the role of the passivation layer as a partial diffusion barrier, improving reproducibility and endurance, as shown by the enhanced LRS/HRS ratio (∼5897.04–∼9526.35) and endurance (from ∼27 543–51 696 cycles) compared to nonpassivated ReRAM device structures [27]. Furthermore, the insulating nature of the HfO_X resulted in an approximately threefold reduction in both HRS and LRS current densities, enhancing device reliability and longevity. Collectively, these effects render HfO_X an effective interfacial passivation layer for improving the reliability and switching consistency of $AgEuBr_4$-based ReRAM devices.

To further elucidate the filamentary conduction mechanism, additional control experiments were conducted by substituting the active Ag TE with inert Pt, creating $Pt/AgEuBr_4/FTO$ and $Pt/HfO_X/AgEuBr_4/FTO$ devices under identical processing conditions. The resulting dual-sweep current density–voltage ($J-V$) characteristics, depicted in Fig. 3(e) and (f), exhibited distinctly different switching behavior compared to their Ag-TE counterparts. Both Pt-based configurations displayed gradual, analog-like modulation without pronounced SET or RESET transitions, indicative of nonfilamentary, interface-limited conduction mechanisms. These observations strongly

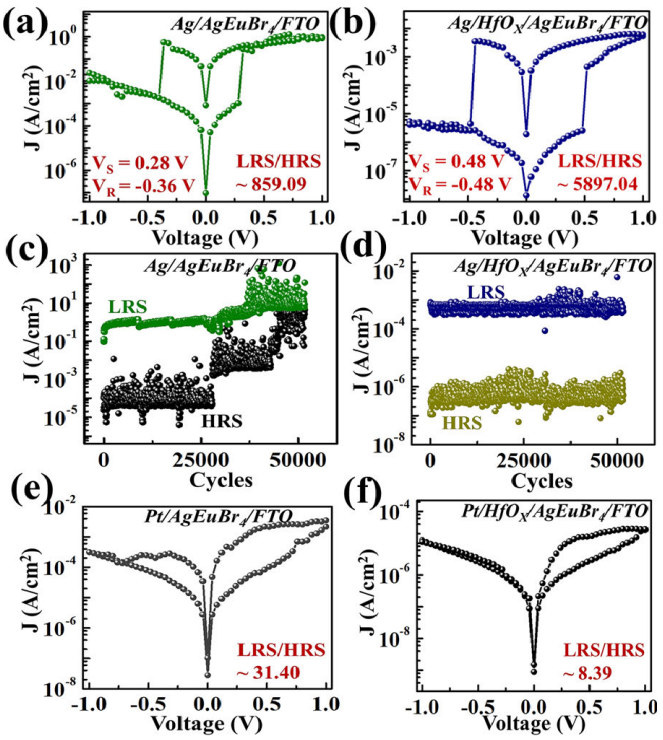

Fig. 3. (a) $J-V$ RS characteristic of $Ag/AgEuBr_4/FTO$ ReRAM. (b) $J-V$ RS characteristic of $Ag/HfO_X/AgEuBr4/FTO$, ReRAM. (c) Endurance performance of Ag/AgEuBr4/FTO ReRAM. (d) Endurance performance of $Ag/HfO_X/AgEuBr4/FTO$ ReRAM. (e) $J-V$ RS characteristic of Pt/AgEuBr4/FTO ReRAM. (f) $J-V$ RS characteristic of $Pt/HfO_X/AgEuBr_4/FTO$ ReRAM.

support the hypothesis that RS in Ag-based devices primarily arises from electrochemical redox reactions involving Ag^+ ion migration and subsequent metallic CF formation. In addition, Fig. 3(e) and (f) shows that the $Pt/AgEuBr_4/FTO$ configuration exhibited a hysteresis loop with an LRS/HRS ratio of ∼31.40 during positive voltage sweeps, whereas the hysteresis loop significantly reduced to ∼8.39 in the $Pt/HfO_X/AgEuBr_4/FTO$ configuration. This reduced hysteresis confirms the passivation effect on surface trap states.

After affirming the role of passivating $AgEuBr_4$ SL under HfO_X thin layer, the fabricated Ag/HfOx/$AgEuBr_4$/FTO ReRAM devices were also tested under the UV (λ = 365 nm) irradiation and achieved two more distinct resistive states through photon excitations. The experimental setup customized for the electrical characterization of the fabricated ReRAM devices is illustrated in Fig. 4(a). A dc voltage bias was applied through the Ag TE, while the FTO BE was maintained at ground potential. To assess the phototunable behavior of the devices, UV irradiation was directed onto the FTO side of the ReRAM stack using a calibrated UV source. The source was positioned at a fixed distance to maintain a constant irradiation intensity of 352 $\mu W/cm^2$ throughout the measurement process.

The RS behavior of the $Ag/HfO_X/AgEuBr_4/FTO$ ReRAMs was evaluated via current density–voltage ($J-V$) analysis under both dark and UV-irradiated conditions. As shown in Fig. 4(b), a symmetric dc voltage sweep protocol of

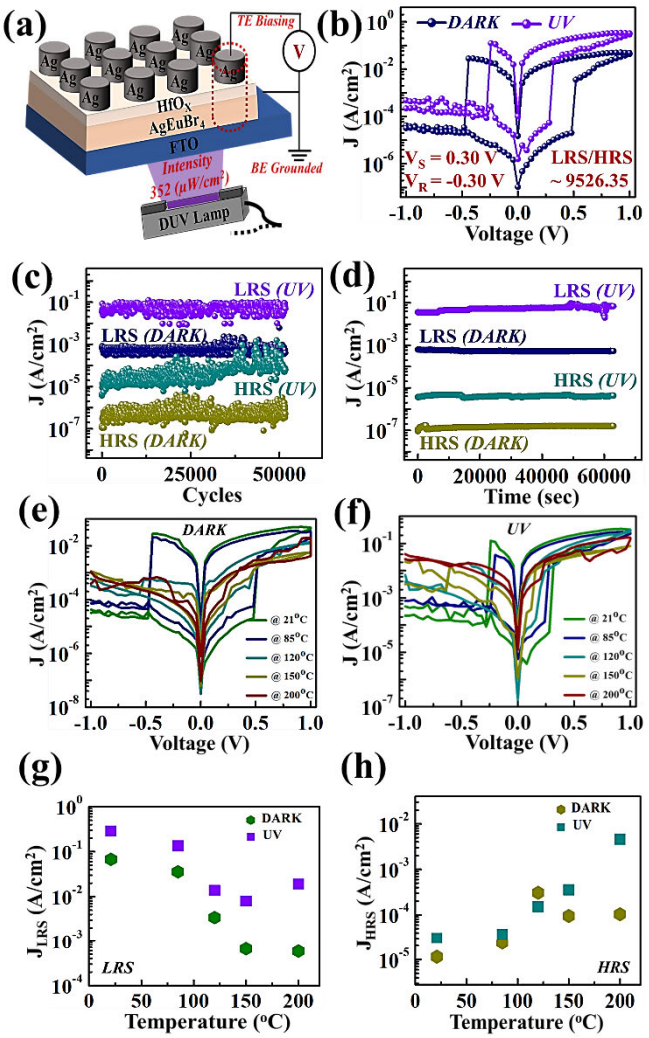

Fig. 4. (a) 3-D schematic illustration of the customized experimental setup. (b) $J-V$ RS characteristics of Ag/HfO_X/$AgEuBr_4$/FTO ReRAM under dark and UV irradiations. (c) Endurance performance under dark and UV irradiation. (d) Retention characteristics under dark and UV irradiation. $J-V$ characteristics of the fabricated Ag/HfO_x/$AgEuBr_4$/FTO ReRAM at various temperatures under the operating conditions of (e) dark and (f) UV irradiations. Temperature-dependent current densities under the dark and UV irradiation. (g) LRS. (h) HRS.

$-1\ \text{V} \rightarrow 0\ \text{V} \rightarrow +1\ \text{V} \rightarrow 0\ \text{V} \rightarrow -1\ \text{V}$ was applied to analyse the bipolar switching characteristics. Under dark conditions, the device exhibited LRS/HRS ~5897.04 while operating at $V_S = +0.48$ V and $V_R = -0.48$ V. Upon exposure to UV irradiation, the RS characteristics were significantly enhanced. V_S and V_R were reduced to +0.30 and −0.30 V, respectively, and the LRS/HRS current ratio improved to ~9526.35. The observed improvements under UV irradiation can be attributed to the photogenerated charge carriers enhancing ionic mobility and reducing energy barriers for Ag-CF formation and rupture processes. This phenomenon, commonly referred to as photon-enhanced cationic/ionic migration, promotes more efficient and low-voltage switching by activating and facilitating charge transport pathways in perovskite-based systems [1], [2]. Quantitatively, UV irradiations reduced the operating voltages by approximately 1.60 times and increased the LRS/HRS ratio by 1.61 times. Thus, such shifts in the resistances of the ReRAM devices under UV irradiations provide two more different resistive states while employing photonic excitations. Also, the enhancements in the ReRAM switching confirm the phototunability of the Ag/HfO_X/$AgEuBr_4$/FTO ReRAMs, positioning them as promising candidates for multifunctional optoelectronic memory applications. The observed optically assisted switching behavior aligns well with the mechanisms of photon-enhanced ionic migration and defect activation reported in perovskite-based systems [1], [2], [28].

The endurance and long-term retention tests were conducted to evaluate the nonvolatile memory (NVM) characteristics of the fabricated Ag/HfO_X/$AgEuBr_4$/FTO ReRAM devices under UV irradiations and were compared with the dark condition results. In both cases (dark and UV irradiation), the fabricated ReRAM shows excellent endurance characteristics and follows nonoverlapping of LRS and HRS states up to the conducted 51 696 cycles. After programming the devices into their SET and RESET states, a constant read voltage of 0.1 V was applied to monitor the stability of both resistance states over time.

As shown in Fig. 4(d), the device exhibited excellent data retention, maintaining a stable LRS and HRS with an LRS/HRS ratio of ~5897.04 (dark) and ~9526.35 (UV) for 62 986-s test durations. This indicates that the conformal HfO_X interface acts as an ion-confining barrier layer, limiting filament relaxation and suppressing lateral diffusion [23], [27]. In addition, the long-term endurance and retention also suggest that the defect-tolerant and chemically active nature of $AgEuBr_4$ supports electrochemical Ag^+ reduction, and filament nucleation facilitates stable anchoring of Ag filaments. These factors collectively mitigate the volatility typically observed in nonpassivated Ag-filament systems [29].

To further assess thermal robustness, we evaluated the temperature-dependent stability of Ag/HfO_X/$AgEuBr_4$/FTO ReRAM devices at elevated temperatures—21 °C °C, 85 °C, 120 °C, 150 °C, and 200 °C using a Linkam heating stage while maintaining constant humidity of ~45%. Electrical $J-V$ measurements were performed under both dark and UV ($\lambda \sim 365$ nm) irradiation. The corresponding $J-V$ characteristics are presented in Fig. 4(e) and (f), while the extracted temperature-dependent current density variations for the low-resistance state (J_{LRS}) and high-resistance state (J_{HRS}) are summarized in Fig. 4(g) and (h), respectively. As the temperature increased, J_{LRS} exhibited a continuous decrement, consistent with the metallic nature of Ag CFs [30], [31], whose electrical conductivity typically reduces with rising temperature due to enhanced electron–phonon scattering, a hallmark of metallic transport. Compared to 21 °C, J_{LRS} decreased only 1.89X under dark and 2.14X under UV at 85 °C, indicating robust filament confinement and thermal stability. However, beyond 85 °C, J_{LRS} sharply declined by 19.73X, 103.09X, and 116.10X under dark at 120 °C, 150 °C, and 200 °C, respectively, and by 20.93X, 36.16X, and 15.22X under UV. This acute reduction is not attributed to $AgEuBr_4$ phase instability, as the material was thermally annealed at 260 °C during the fabrication process flow and remains structurally stable within this range. Instead, the observed decline in J_{LRS} beyond 85 °C is likely due to thermally accelerated Ag^+ ion diffusion and CF

relaxation at the Ag/HfO_X interface. In addition, the elevated temperatures can promote atomic migration, electromigration-induced drift, or partial filament rupture, leading to increased filament resistance or discontinuity [30], [31].

Conversely, J_{HRS} increased with rising temperature, which is attributed to thermally activated trap-assisted tunneling and enhanced intrinsic carrier excitation in the $AgEuBr_4$ layer. At 85 °C, J_{HRS} increased modestly by 2.04X (dark) and 1.21X (UV). More pronounced increases were observed at higher temperatures: 26.84X (dark) and 5.02X (UV) at 120 °C; 8.26X (dark) and 11.69X (UV) at 150 °C; and 9.04X (dark) and 15.2X (UV) at 200 °C. Under UV illumination, additional photogenerated carriers likely lower the interfacial barrier and enhance conduction through defect states in the high-resistance regime [32]. The opposite trends in J_{HRS} and J_{LRS} with increasing temperature further support the presence of a metallic Ag filament-based switching mechanism [33], [34], where LRS is governed by ohmic transport through Ag CFs, while HRS is dominated by thermally activated leakage across the semiconducting matrix. These results confirm that the HfO_X-passivated $AgEuBr_4$ ReRAM devices retain excellent thermal stability up to 85 °C, with functional retention of nonvolatile states under both dark and UV illumination, thereby supporting their potential operation in a real-world ambient environment. However, degradation at temperatures ≥120 °C highlights the need for further electrode and interface engineering, optimization, and thermal stability analysis for future iterations.

Following the confirmation of superior RS characteristics in Ag/HfO_X/$AgEuBr_4$/FTO ReRAM devices, their potential for neuromorphic computing applications was further examined by investigating synaptic learning behaviors. A key functionality required for artificial synapses is the capability to modulate conductance linearly and gradually in response to external stimuli, thereby emulating biological synaptic plasticity. To assess this functionality, pulse-driven conductance modulation experiments were performed. A train of 100 consecutive identical voltage pulses, each with an amplitude of ±0.5 V, a pulsewidth (T_P) of 100 ns, and an interpulse interval of 100 ns, was applied to the fabricated devices. The switching durations, derived from the 100th $V-I-T$ pulse plots, were determined to be 10.16 ns under dark conditions and 10.07 ns under UV illumination, as depicted in Fig. 5(a) and (b).

From a neurobiological perspective, synaptic plasticity is generally categorized into short-term plasticity (STP) and long-term potentiation (LTP). STP primarily governs rapid neuronal communication and temporal information encoding, while LTP underlies the fundamental mechanisms of learning and long-term memory consolidation. The evolution of conductance (G) with the number of applied pulses was systematically monitored to evaluate the device's ability to replicate LTP. Under dark conditions, the device exhibited a smooth and continuous increase in conductance during potentiation (positive pulses), reaching G = 8.8 × 10^{-4}S, and a gradual decrease during depression (negative pulses), resulting in a nearly linear G–G-pulse profile without abrupt transitions or saturation effects. Here, the brief pulses (T_P = 100 ns) induce partial and incremental modulation of CFs at the applied amplitude of ±0.5 V, yielding gradual,

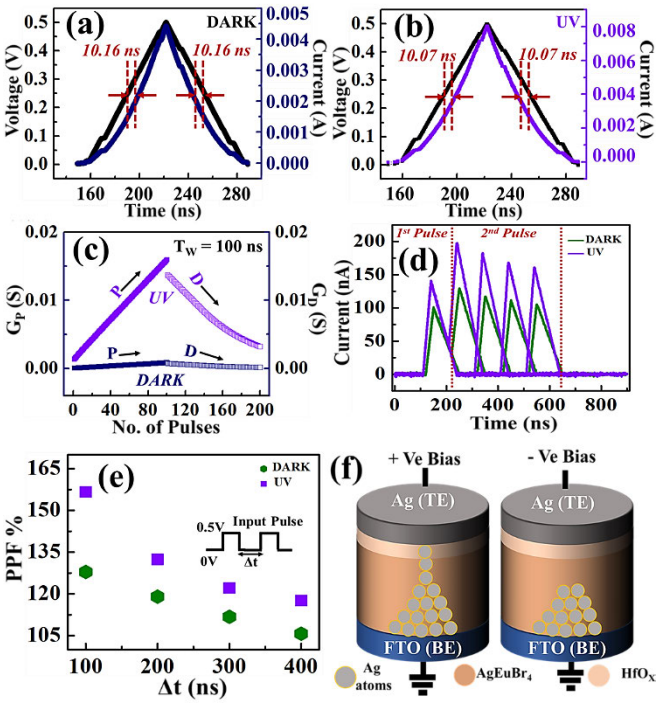

Fig. 5. (a) *V-I-T* (voltage–current–time) pulse response of Ag/HfO_X/$AgEuBr_4$/FTO ReRAM under dark conditions. (b) *V-I-T* pulse response under UV (λ = 365 nm) irradiation. (c) Pulse-driven conductance modulation demonstrating potentiation and depression under dark and UV conditions. (d) PPF effect obtained in ReRAM by applying two paired pulses (0.5 V, 100 ns) at four different intervals. (e) PPF percentage as a function of pulse interval. (f) Schematic illustration of Ag CF formation and rupture in Ag/HfO_X/$AgEuBr_4$/FTO ReRAM.

analog-like conductance tuning [see Fig. 5(c)], in contrast to the abrupt SET/RESET transitions observed in dc $I-V$ sweeps [see Fig. 3(b)] arising from full formation and rupture of Ag CFs under slow, continuous bias. This analog switching behavior, free from overshoot or instability, is highly desirable for neuromorphic hardware implementations. Such dual-mode switching behavior—digital under dc and analog under pulsed stimuli—is well-documented in memristive systems [35], [36] and reflects the underlying electrochemical kinetics governed by stimulus amplitude and duration conditions.

Subsequently, the same pulsing protocol was repeated under continuous UV illumination (λ = 365 nm and intensity = 352 μW/cm^2) to examine the influence of photonic excitation on synaptic modulation. Under UV exposure, a significantly enhanced conductance response was observed, especially during the potentiation phase, i.e., G = 0.016 S, as shown in Fig. 5(c). The absence of saturation and the marked increase in peak conductance values under UV conditions indicate improved synaptic weight updating, suggesting an optically enhanced plasticity mechanism. This enhancement is attributed to the synergistic effect of photo-generated carriers and Ag ion migration within the SL. UV photon absorption at the HfO_X/$AgEuBr_4$ interface generates additional electron–hole pairs, which locally modulate the electric field and facilitate charge carrier transport. Simultaneously, UV irradiation increases the mobility of Ag+ ions, promoting more efficient and controlled formation of CFs. Together, these effects

dynamically tune the device's conductance, offering finer control over synaptic weight modulation, a critical requirement for optoelectronic neuromorphic systems.

To investigate STP, a fundamental feature of biological learning, we conducted paired-pulse facilitation (PPF) measurements using a series of voltage-paired pulses (0.5 V, 100 ns width) with varying interpulse intervals (Δt = 100–400 ns). The PPF index, calculated as the ratio of the second excitatory postsynaptic current (EPSC) amplitude (A2) to the first (A1), serves as an indicator of the synapse's ability to retain temporal information. This phenomenon is widely observed in neuroscience, where a closely spaced second stimulus often leads to a stronger postsynaptic response due to residual presynaptic activity [37]. As illustrated in Fig. 5(d), the fabricated Ag/HfO_X/$AgEuBr_4$/FTO memristor exhibited a clear PPF effect, with the amplitude of the second EPSC strongly influenced by the time interval between pulses [3], [8], [29]. Under dark conditions, the first pulse induced an EPSC of 98.38 nA, while the second EPSC progressively decreased from 125.93 to 104.05 nA as Δt increased from 100 to 400 ns. A similar trend was observed under UV irradiation, where the initial EPSC was 115.47 nA, and the second EPSC dropped from 180.81 to 135.52 nA with increasing pulse intervals. This reduction in facilitation with longer delays is consistent with the transient memory decay characteristics of biological synapses. Therefore, as shown in Fig. 5(e), the device exhibited a decreasing PPF% with increasing Δt, consistent with the characteristic memory decay behavior observed in biological synapses. Notably, under UV irradiations, the device exhibited an enhanced PPF%, attributed to photoinduced carrier generation and improved Ag^+ ion mobility, which collectively facilitate more efficient paired-pulse transmission. Even at larger Δt values, the PPF% under UV remained higher than in dark conditions, with enhancements of 1.22X, 1.13X, 1.09X, and 1.11X at Δt values of 100, 200, 300, and 400 ns, respectively. This enhanced PPF% under UV is a desirable feature, as it reflects improved synaptic responsiveness and greater short-term memory retention, which are essential for mimicking dynamic signal processing in biological neural networks. In neuromorphic systems, higher PPF indicates stronger facilitation during high-frequency spiking activity, enabling more accurate emulation of sensory perception and associative learning [3], [8], [29]. These results confirm that photon-assisted ionic transport and charge dynamics contribute to improved STP and LTP facilitation, demonstrating the phototunable neuromorphic capability of the Ag/HfO_X/$AgEuBr_4$/FTO ReRAM systems.

As shown in Fig. 5(a), the formation of Ag CFs enables potentiation during the application of consecutive positive voltage pulses. This follows the electrochemical reduction of Ag^+ ions to Ag atoms ($Ag^+ + e^- \rightarrow$ Ag) [1], [30], [38] at the $AgEuBr_4$/FTO interface, facilitating the growth of the Ag atoms from BE to TE and resulting in incrementally increased conductance. Conversely, depression occurs under negative voltage pulses [see Fig. 5(b)], which induces the oxidation of Ag atoms to Ag^+ ions as $Ag \rightarrow Ag^+ + e^-$, rupturing the CFs and decreasing conductance. A schematic representation of Ag filament formation and rupture is provided in Fig. 5(f).

These findings position the Ag/HfOx/$AgEuBr_4$/FTO ReRAM as a highly promising optoelectronic memristive platform for neuromorphic computing applications. Its capability to achieve linear, nonvolatile, and photon-modulated conductance updates makes it particularly well-suited for enabling energy-efficient, bioinspired computational architectures.

IV. Conclusion

In summary, this work presents a novel lead-free perovskite-inspired lanthanohalide, $AgEuBr_4$, as a highly efficient SL for phototunable ReRAM devices. The robust Ag/HfO_X/$AgEuBr_4$/FTO architecture was fabricated using a fully dry process that leverages the use of an indigenously custom-designed and developed In-MAA MOC-based negative PR. This cutting-edge, solvent-free dry development method ensures unparalleled precision in patterning the silver (Ag) electrodes. The devices exhibited stable bipolar RS with impressively low operating voltages ($\pm$0.48 V in dark and $\pm$0.30 V under UV) and high LRS/HRS ratios ($\sim$5897.04 in dark and $\sim$9526.35 under UV). Under UV illumination, enhanced conductance modulation was observed during pulse-based synaptic tests (LTP and STP), confirming the phototunable nature of $AgEuBr_4$ and its suitability for neuromorphic applications. The Ag/HfO_X/$AgEuBr_4$/FTO ReRAM demonstrated ultrafast switching while transitioning from LRS to HRS and vice versa at a switching duration of 10.16 ns (dark) and 10.07 ns (UV). Overall, the integration of $AgEuBr_4$ as a photoreactive switching material, along with the novel fabrication strategy, demonstrates a promising platform for optoelectronic memory and artificial synapse devices, making it an ideal candidate for transformative neuromorphic applications.

Acknowledgment

The authors acknowledge the Centre for Design and Fabrication of Electronic Devices (C4DFED) and the Class 100 Cleanroom Facility at the IIT Mandi, India, for their support in sample preparation and electrical characterization. They also acknowledge the state-of-the-art FESEM facility available in C4DFED for nanoscale imaging and the chemical characterization facilities at the Advanced Material Research Center (AMRC), IIT Mandi.

References

[1] M. Chauhan, R. Singh, and S. K. Sharma, "Electro-optically tunable passivated double-cation perovskite-based ReRAM for low-power memory applications," *ACS Appl. Electron. Mater.*, vol. 6, no. 4, pp. 2709–2719, Apr. 2024, doi: 10.1021/acsaelm.4c00257.

[2] R. Ray and S. K. Pal, "Solution-processed photoinduced multilevel resistive switching devices based on lead-free all-inorganic perovskite," *IEEE Electron Device Lett.*, vol. 42, no. 9, pp. 1284–1287, Sep. 2021, doi: 10.1109/LED.2021.3094895.

[3] H. Sun et al., "Optoelectronic synapses based on a triple cation perovskite and Al/MoO_3 interface for neuromorphic information processing," *Nanosc. Adv.*, vol. 6, no. 2, pp. 559–569, Jan. 2024, doi: 10.1039/d3na00677h.

[4] G. Grancini and M. K. Nazeeruddin, "Dimensional tailoring of hybrid perovskites for photovoltaics," *Nature Rev. Mater.*, vol. 4, no. 1, pp. 4–22, Nov. 2018, doi: 10.1038/s41578-018-0065-0.

[5] P. Kumar, S. K. Sharma, and R. Singh, "A hydrophobic organic spacer cation for improving moisture resistance and efficiency in mixed-dimensional perovskite solar cells," *EES Sol.*, vol. 1, no. 3, pp. 356–365, 2025, doi: 10.1039/d5el00034c.

[6] M. Kundar, P. Kumar, S. K. Sharma, R. Singh, and S. K. Pal, "Stable perovskite solar cells based on direct surface passivation employing 2D perovskites," *Sol. RRL*, vol. 7, no. 23, pp. 1–11, Dec. 2023, doi: 10.1002/solr.202300572.

[7] A. Wang, C. Zuo, X. Niu, L. Ding, J. Ding, and F. Hao, "Recent promise of lead-free halide perovskites in optoelectronic applications," *Chem. Eng. J.*, vol. 451, Jan. 2023, Art. no. 138926, doi: 10.1016/j.cej.2022.138926.

[8] Z. Liu et al., "Inorganic lead-free and bismuth-based perovskite nanoscale-thick films for memristors and artificial synapse applications," *ACS Appl. Nano Mater.*, vol. 6, no. 22, pp. 21000–21015, Nov. 2023, doi: 10.1021/acsanm.3c04006.

[9] Z. Liu et al., "High-performance and environmentally robust multilevel lead-free organotin halide perovskite memristors," *Adv. Electron. Mater.*, vol. 9, no. 1, Jan. 2023, Art. no. 2201005, doi: 10.1002/aelm.202201005.

[10] G. S. H. Thien et al., "Recent advances in halide perovskite resistive switching memory devices: A transformation from lead-based to lead-free perovskites," *ACS Omega*, vol. 7, no. 44, pp. 39472–39481, Nov. 2022, doi: 10.1021/acsomega.2c03206.

[11] J. Huang et al., "Lead-free cesium europium halide perovskite nanocrystals," *Nano Lett.*, vol. 20, no. 5, pp. 3734–3739, May 2020, doi: 10.1021/acs.nanolett.0c00692.

[12] J. Li et al., "Highly efficient and air-stable Eu(II)-containing azacryptates ready for organic light-emitting diodes," *Nature Commun.*, vol. 11, no. 1, p. 5218, Oct. 2020, doi: 10.1038/s41467-020-19027-x.

[13] M. Pazoki, A. Röckert, M. J. Wolf, R. Imani, T. Edvinsson, and J. Kullgren, "Electronic structure of organic–inorganic lanthanide iodide perovskite solar cell materials," *J. Mater. Chem. A*, vol. 5, no. 44, pp. 23131–23138, 2017, doi: 10.1039/c7ta07716e.

[14] T. Tong et al., "Rare Earth halide double perovskites for high-performance resistive random access memory," *J. Mater. Chem. C*, vol. 11, no. 14, pp. 4946–4952, 2023, doi: 10.1039/d3tc00350g.

[15] A. Chakraborty, N. Pai, J. Zhao, B. R. Tuttle, A. N. Simonov, and V. Pecunia, "Rudorffites and beyond: Perovskite-inspired silver/copper pnictohalides for next-generation environmentally friendly photovoltaics and optoelectronics," *Adv. Funct. Mater.*, vol. 32, no. 36, Sep. 2022, Art. no. 2203300, doi: 10.1002/adfm.202203300.

[16] L. Staišiūnas et al., "Silicon passivation by ultrathin hafnium oxide layer for photoelectrochemical applications," *Frontiers Chem.*, vol. 10, pp. 1–10, Mar. 2022, doi: 10.3389/fchem.2022.859023.

[17] R. Zhao et al., "Surface passivation of organometal halide perovskites by atomic layer deposition: An investigation of the mechanism of efficient inverted planar solar cells," *Nanosc. Adv.*, vol. 3, no. 8, pp. 2305–2315, Apr. 2021, doi: 10.1039/d1na00075f.

[18] P. Chen et al., "Interfacial passivation by using an amorphous hafnium oxide thin layer toward improved $CH_3NH_3PbI_3$/Si heterojunction photodetectors," *Appl. Phys. Lett.*, vol. 125, no. 10, Sep. 2024, Art. no. 103301, doi: 10.1063/5.0221884.

[19] Z. Xing et al., "Atomic layer deposition of metal oxides in perovskite solar cells: Present and future," *Small Methods*, vol. 4, no. 12, pp. 1–9, Dec. 2020, doi: 10.1002/smtd.202000588.

[20] L. Tian, K. Sun, Y. Rui, W. Cui, and W. An, "Facile synthesis of an Ag@AgBr nanoparticle-decorated $K_4Nb_6O_{17}$ photocatalyst with improved photocatalytic properties," *RSC Adv.*, vol. 8, no. 51, pp. 29309–29320, 2018, doi: 10.1039/c8ra03597k.

[21] N. K. Eswar, V. V. Katkar, P. C. Ramamurthy, and G. Madras, "Novel AgBr/Ag_3PO_4 decorated ceria nanoflake composites for enhanced photocatalytic activity toward dyes and bacteria under visible light," *Ind. Eng. Chem. Res.*, vol. 54, no. 33, pp. 8031–8042, Aug. 2015, doi: 10.1021/acs.iecr.5b01993.

[22] X.-Y. Zhang et al., "Crystallinity effect on electrical properties of PEALD–HfO_2 thin films prepared by different substrate temperatures," *Nanomaterials*, vol. 12, no. 21, p. 3890, Nov. 2022, doi: 10.3390/nano12213890.

[23] G. Bersuker et al., "Grain boundary-driven leakage path formation in HfO_2 dielectrics," *Solid-State Electron.*, vols. 65–66, pp. 146–150, Nov. 2011, doi: 10.1016/j.sse.2011.06.031.

[24] M. Chauhan, K. Palit, S. Choudhary, S. K. Sharma, and K. E. Gonsalves, "Ultrasensitive metal-organic cluster resist for patterning of single exposure high numerical aperture extreme ultraviolet lithography applications," *J. Micro/Nanopatterning, Mater., Metrology*, vol. 21, no. 4, Dec. 2022, Art. no. 044603, doi: 10.1117/1.jmm.21.4.044603.

[25] E. C. Mattson et al., "Chemical modification mechanisms in hybrid hafnium Oxo-methacrylate nanocluster photoresists for extreme ultraviolet patterning," *Chem. Mater.*, vol. 30, no. 17, pp. 6192–6206, Sep. 2018, doi: 10.1021/acs.chemmater.8b03149.

[26] J. Xian, H. Zhou, M. Zhou, and X. Zhang, "A novel O_2/N_2 plasma photoresist ashing process with high stripping rate and uniformity under radio frequency bias voltage," in *Proc. 25th Int. Conf. Electron. Packag. Technol. (ICEPT)*, Aug. 2024, pp. 1–6, doi: 10.1109/icept63120.2024.10668447.

[27] S. Biswas et al., "Impact of AlO_y interfacial layer on resistive switching performance of flexible HfO_x/AlO_y ReRAMs," *IEEE Trans. Electron Devices*, vol. 68, no. 8, pp. 3787–3793, Aug. 2021, doi: 10.1109/TED.2021.3084554.

[28] T. Paul, P. K. Sarkar, S. Maiti, and K. K. Chattopadhyay, "Multilevel programming and light-assisted resistive switching in a halide-tunable all-inorganic perovskite cube for flexible memory devices," *ACS Appl. Electron. Mater.*, vol. 2, no. 11, pp. 3667–3677, Nov. 2020, doi: 10.1021/acsaelm.0c00719.

[29] Z. Wang et al., "Memristors with diffusive dynamics as synaptic emulators for neuromorphic computing," *Nature Mater.*, vol. 16, no. 1, pp. 101–108, Jan. 2017, doi: 10.1038/nmat4756.

[30] Q. Liu et al., "Real-time observation on dynamic growth/dissolution of conductive filaments in oxide-electrolyte-based ReRAM," *Adv. Mater.*, vol. 24, no. 14, pp. 1844–1849, Apr. 2012, doi: 10.1002/adma.201104104.

[31] N. Singh and D. Kaur, "Origin of tri-state resistive switching characteristics in SiCN thin films for high-temperature ReRAM applications," *Appl. Phys. Lett.*, vol. 113, no. 16, p. 2103, Oct. 2018, doi: 10.1063/1.5045723.

[32] K. Jiang, Z. Zheng, S. Hu, Z. Zhao, and H. Wang, "Recent progress in brain-like chips based on optoelectronic memory: Structures, mechanisms, and prospects," *Appl. Phys. Rev.*, vol. 12, no. 2, Jun. 2025, Art. no. 021322, doi: 10.1063/5.0230269.

[33] Z. Wang et al., "Resistive switching materials for information processing," *Nature Rev. Mater.*, vol. 5, no. 3, pp. 173–195, 2020, doi: 10.1038/s41578-019-0159-3.

[34] I. Valov, R. Waser, J. R. Jameson, and M. N. Kozicki, "Electrochemical metallization memories—Fundamentals, applications, prospects," *Nanotechnology*, vol. 22, no. 28, Jul. 2011, Art. no. 289502, doi: 10.1088/0957-4484/22/28/289502.

[35] B. Gao et al., "Ultra-low-energy three-dimensional oxide-based electronic synapses for implementation of robust high-accuracy neuromorphic computation systems," *ACS Nano*, vol. 8, no. 7, pp. 6998–7004, Jun. 2014, doi: 10.1021/nn501824r.

[36] S. A. Khan and S. Kim, "Comparison of diverse resistive switching characteristics and demonstration of transitions among them in al-incorporated HfO_2-based resistive switching memory for neuromorphic applications," *RSC Adv.*, vol. 10, no. 52, pp. 31342–31347, 2020, doi: 10.1039/d0ra06389d.

[37] R. S. Zucker and W. G. Regehr, "Short-term synaptic plasticity," *Annu. Rev. Physiol.*, vol. 64, no. 1, pp. 355–405, Mar. 2002, doi: 10.1146/annurev.physiol.64.092501.114547.

[38] M. Chauhan, S. Choudhary, and S. K. Sharma, "Reliable memristive switching empowered by Ag/NiO/W ReRAM configuration for multilevel non-volatile memory applications," *Adv. Electron. Mater.*, vol. 10, no. 4, pp. 1–11, Apr. 2024, doi: 10.1002/aelm.202300724.